ARTICLE

Check for updates

Ferroelectric-tuned van der Waals heterojunction with band alignment evolution

Yan Chen[1,2,5], Xudong Wang[1,5], Le Huang[3], Xiaoting Wang[3], Wei Jiang[1], Zhen Wang[1], Peng Wang[1], Binmin Wu[1], Tie Lin[1], Hong Shen [1], Zhongming Wei [3✉], Weida Hu [1,4✉], Xiangjian Meng[1], Junhao Chu[1,2] & Jianlu Wang [1,4✉]

Van der Waals integration with abundant two-dimensional materials provides a broad basis for assembling functional devices. In a specific van der Waals heterojunction, the band alignment engineering is crucial and feasible to realize high performance and multi-functionality. Here, we design a ferroelectric-tuned van der Waals heterojunction device structure by integrating a GeSe/MoS$_2$ VHJ and poly (vinylidene fluoride-trifluoroethylene)-based ferroelectric polymer. An ultrahigh electric field derived from the ferroelectric polarization can effectively modulate the band alignment of the GeSe/MoS$_2$ heterojunction. Band alignment transition of the heterojunction from type II to type I is demonstrated. The combination of anisotropic GeSe with MoS$_2$ realizes a high-performance polarization-sensitive photodetector exhibiting low dark current of approximately 1.5 pA, quick response of 14 μs, and high detectivity of 4.7 × 10^{12} Jones. Dichroism ratios are also enhanced by ferroelectric polarization in a broad spectrum from visible to near-infrared. The ferroelectric-tuned GeSe/MoS$_2$ van der Waals heterojunction has great potential for multifunctional detection applications in sophisticated light information sensing. More profoundly, the ferroelectric-tuned van der Waals heterojunction structure provides a valid band-engineering approach to creating versatile devices.

[1] State Key Laboratory of Infrared Physics, Shanghai Institute of Technical Physics, Chinese Academy of Sciences, Shanghai, China. [2] School of Physics and Electronic Science, East China Normal University, Shanghai, China. [3] State Key Laboratory of Superlattices and Microstructures, Institute of Semiconductors, Chinese Academy of Sciences, Beijing, China. [4] Hangzhou Institute for Advanced Study, University of Chinese Academy of Sciences, Chinese Academy of Sciences, Hangzhou, China. [5] These authors contributed equally: Yan Chen, Xudong Wang. ✉email: zmwei@semi.ac.cn; wdhu@mail.sitp.ac.cn; jlwang@mail.sitp.ac.cn

Heterojunctions are an essential part of functional devices. The integration of different materials guarantees the acquisition of high-performance heterojunctions. Traditional integration strategies, such as chemical and physical epitaxial growth, commonly require harsh preparation conditions and rarely achieve the ideal interface. Interface disorder, chemical contamination, strain, and diffusion effects limit the performance and application of heterostructures[1–3]. Emerging two-dimensional (2D) layered materials provide a state-of-the-art approach to designing heterojunctions based on van der Waals (vdW) interaction. A vdW heterojunction (VHJ) is bond-free integration that is unaffected by the lattice mismatch or the processing condition of materials used. As basic building blocks, various 2D materials exhibit impressive electrical, optical, and magnetic properties[4–6]. Moreover, vdW integration with an atomically clean surface in the heterostructure is notably superior to those of only one material[7,8]. An excellent example is the twisted integration of two monolayer graphene that exhibit unconventional superconductivity and correlated insulator behavior[9,10]. In addition to fundamental physics research, studies have reported that VHJs have excellent potential in high-performance multifunctional devices. Optoelectronic devices, such as photovoltaic photodetectors[11,12] and quantum well LEDs[13], have attracted tremendous research interest because they exhibit remarkably better performance than traditional devices. Electronic devices such as floating-gate memories[14,15] and tunneling diodes[16–20] have exhibited great potential for future applications as well.

With band structure design, the richness of 2D materials and the flexibility of vdW integration provide numerous routes to realize specific functional devices. Typically, three different band alignments can be formed in VHJs: straddling (type I), staggered (type II), and broken (type III). However, multifunctional applications are challenging to achieve with a fixed band alignment. Reliable approaches, like applying an external field[19,21] or controlling the doped element concentration[20,22] band alignment change from type II to type III, can be realized. Thus, Esaki diode and rectifier diode are achieved in VHJs. Woo Jong Yu et al. used an external gate to modulate the band slope and photocurrent generation of graphene-MoS_2-graphene vertical heterostructure with high quantum efficiency[12]. By sufficient controlling of an external electric field, VHJs can achieve robust performance and expand diverse application potentials.

However, tuning of the Fermi levels by the electric field is insufficient to change the band offset, which affects the performance of a heterojunction significantly. Besides, a sustained external voltage to maintain the optimal performance of the device causes considerable power consumption. Ferroelectrics provide a non-volatile remanent polarization electric field over 1 V/nm[23–25], which is large enough to modify the bandgap of semiconductors according to the Stark effect[26–29]. Ferroelectric field-effect transistors based on ferroelectrics and 2D materials have been demonstrated high performances and great potentials in electronics and optoelectronics[30–32]. Predictably, combining ferroelectrics with VHJs achieves highly tunable band structures and tailored optoelectronic properties. Here, we designed a ferroelectric VHJ (Fe-VHJ) consisting of a ferroelectric polymer, P(VDF-TrFE), and GeSe/MoS_2 VHJ. Under modulation of the ferroelectric polarization field, the electrical characteristics of the GeSe/MoS_2 pn junction can be tuned and its output can be maintained at two specific states. The band alignment between GeSe and MoS_2 can be switched from type II (staggered) to type I (straddling) by reversing the direction of ferroelectric polarization field. With ferroelectric-tuned VHJ band engineering, the GeSe/MoS_2 junction can act as a high-performance photodetector. High responsivities are achieved for a wide range of wavelengths

spanning from visible to near-infrared. The anisotropy of GeSe is employed to demonstrate a polarized light-sensitive photodetector, which is further enhanced by the ferroelectric field. More importantly, the ferroelectric field is applied on the VHJ to engineer the band alignment type, broaden the detection wavelength range, and enrich functionalities.

Results and discussion

Fabrication of GeSe/MoS_2 Fe-VHJ. The device structure we designed is depicted in Fig. 1a. GeSe and MoS_2 form the VHJ, in which GeSe is an anisotropic 2D semiconductor. Unlike MoS_2, which has an in-plane hexagonal structure, GeSe has a rectangular structure in the plane, that is, different structures in the x and y directions. It has an "armchair" shape along the x-axis and a "zigzag" shape along the y-axis. The specific atomic structure of GeSe is illustrated in Supplementary Fig. 1. Because of its anisotropic structure, GeSe possesses electrical anisotropy and optical linear dichroism, which satisfies its application in polarized light detection. P(VDF-TrFE) is covered on the GeSe/MoS_2 VHJ. Here we apply it to engineer the band structure and enhance the optoelectronic performance of the VHJ. The band structure of GeSe and MoS_2 is shown in Fig. 1b. The bottom of the conduction band and the top of the valence band of GeSe (MoS_2) are approximately −4.1 eV (−4.2 eV) and −5.2 eV (−5.4 eV)[33]. The offsets of the conduction band and valence band are approximately 0.1 and 0.2 eV, respectively. Therefore, a type II band alignment is formed, which is beneficial for separating photo-generated carriers and achieving high-speed photoresponse. Figure 1c is an optical micrograph of the device. Electrodes are situated near the boundary of the overlapped heterojunction to eliminate the effect of series resistance. The heterostructure composed of GeSe and MoS_2 is well assembled, as confirmed by Raman spectra and transmission electron microscopy (TEM). As shown in Fig. 1d, the heterostructure exhibits Raman characteristic peaks of both GeSe and MoS_2. The peaks at 150.6 and 187.4 cm^{-1} represent the out-of-plane vibration mode (B_{3g}) and in-plane vibration mode (A_g) of GeSe, respectively. The other two peaks at 383.5 cm^{-1} (in-plane vibration mode E^1_{2g}) and 407.5 cm^{-1} (out-of-plane vibration mode A_{1g}) belong to MoS_2. The cross-section of the heterojunction observed by TEM is displayed in Fig. 1e. The thickness of GeSe is approximately 120 nm, and that of MoS_2 is approximately 6 nm. The GeSe nanoflake is relatively thick for better light absorption, and the thin MoS_2 is chosen for the effective collection of photo-generated electrons. A similar design has been reported in BP/MoS_2 photodetectors[34]. The vdW integration of GeSe and MoS_2 does not exhibit mismatch or pinning on the interface, thus guaranteeing high electrical performance. In this device, a thin amorphous layer is observed in the high-resolution image of the GeSe/MoS_2 interface (Fig. 1f). This layer possibly originates from the exfoliation-restack process, which may hinder the separation of photo-generated carriers and delay the response time[34]. The corresponding feature element maps obtained through energy-dispersive X-ray spectroscopy depict the spatial distribution of GeSe and MoS_2.

Electrical properties and operation mechanism of the device. As depicted in Fig. 2a, the device configuration consists of three functional parts in a series-resistance mode: a p-type GeSe ferroelectric field-effect transistor (p-FeFET), an n-type MoS_2 ferroelectric field-effect transistor (n-FeFET), and a GeSe/MoS_2 Fe-VHJ. We can decide which one is dominant by changing the gate or bias voltage. Figure 2b presents a micrograph of the device; the highlighted portion represents the actual test area, corresponding to the three parts in Fig. 2a. From the output curves in Supplementary Fig. 2, both MoS_2 and GeSe are well-contacted with their electrodes, indicating that the Schottky barrier has little effect on
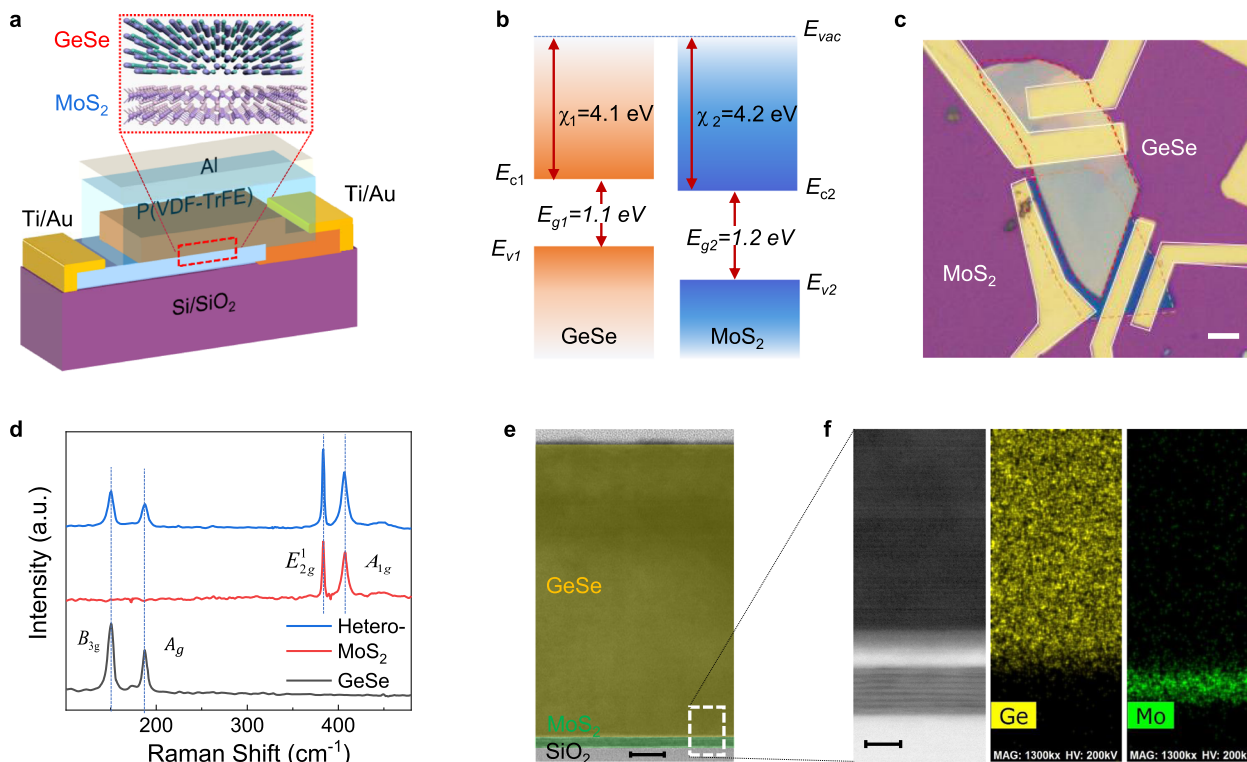
Fig. 1 Design and characterization of GeSe/MoS₂ heterojunction. a Schematic illustration of the GeSe/MoS$_2$ heterojunction with the P(VDF-TrFE) gate. **b** Energy bands of GeSe and MoS$_2$ before contact. χ_1, χ_2, E_{g1}, and E_{g1} are from related literatures. **c** Optical micrograph of the heterojunction; scale bar: 5 μm. **d** Raman spectra of GeSe and MoS$_2$ and their overlap. **e** TEM image of the heterostructure; scale bar: 10 nm. **f** High-resolution cross-sectional image of the GeSe/MoS$_2$ interface and the corresponding chemical element distribution; scale bar: 5 nm.

the electrical performance of the VHJ. The transfer characteristics of n-type MoS$_2$ and p-type GeSe gated by P(VDF-TrFE) are portrayed in Fig. 2c, which shows the same hysteresis direction. The transfer curve of MoS$_2$ exhibits ferroelectric hysteresis, whereas that of GeSe does not. The counter-clockwise hysteresis of GeSe originates from charge injection or carriers capture by trap sites. Due to the interface trap states, a large hysteresis window is found in the transfer curve of a GeSe FET tuned by SiO$_2$ back gate (Supplementary Fig. 3b). By contrast, under the modulation of P(VDF-TrFE) top gate, part of the trap states is localized by the polarization field, thereby narrowing the hysteresis window (Supplementary Fig. 3a). Furthermore, two peaks in gate current are generated by polarization state reverse. So, the polarization electric field is indeed applied to the channel. The ferroelectric electric field (~1.2 V/nm) is giant enough to modulate the intrinsic carrier concentration ($n_i \propto \exp(-E_g/2kT)$) and broaden the photoresponse spectral range as shown in Supplementary Figs. 4 and 5. Therefore, the P(VDF-TrFE) is supposed to modulate the band structure of GeSe. Detailed DFT calculations and experimental analysis are provided in Supplementary Figs. 6–8 and Supplementary Notes 1 and 2. The transfer characteristics of the VHJ gated by P(VDF-TrFE) are shown in Fig. 2d. In the device configuration, the heterojunction is in series with MoS$_2$ and GeSe, so the transfer characteristics of the device are also co-modulated by MoS$_2$ and GeSe nanoflakes. The ferroelectric hysteresis is observed in the transfer curves at a forward bias (1 V) and a reverse bias (−1 V). The transport plots can be sorted into two parts. When V_{tg} sweeps from −40 to 20 V and from −20 to −40 V, P(VDF-TrFE) polymer is polarized up (P$_{up}$) and MoS$_2$ channel is fully depleted, which turns off the entire channel and results in the smallest I_d. When V_{tg} sweeps from 40 to −20 V and from 20 to 40 V, P(VDF-TrFE) polymer is polarized down (P$_{down}$), the MoS$_2$ channel is turned on and most V_d

loads on the p-type GeSe part. As a result, holes in GeSe domain the electrical properties of the channel and the drain current increases when the gate voltage sweeps from 40 to −20 V. Therefore, the carrier concentration of the Fe-VHJ is modulated by polarization field, and the device can maintain two states without external gate voltage. Figure 2e shows the output characteristics at three states: "Fresh", "P$_{up}$", and "P$_{down}$", corresponding to the different polarization states of P(VDF-TrFE). At the Fresh state, the GeSe/MoS$_2$ junction acts as a *pn* diode, but its rectification ratio is small. The ferroelectric polarization states have considerable impacts on reverse current, whereas forward current remains almost unchanged. The changes in the reverse current may result from the band structure transform at the heterojunction interface.

The experimental determination of band structures of semiconductors and heterojunctions includes optical techniques[28,35], photoemission spectroscopy[28,36–38], and electrical transport techniques[39,40]. For the limitation of materials and device structure, the photoemission and optical techniques are not suitable for our device. Here, we analyze the band structure evolution with polarization electric field from the electrical transport properties and the phenomena model is built in Figs. 2f–h. At the fresh state, GeSe and MoS$_2$ formed a type II heterojunction, which is conducive to photo-generated carrier separation. According to Fig. 1b, the band offsets of the conduction bands and the valence bands are 0.10 and 0.20 eV, respectively. In this GeSe/MoS$_2$ VHJ, the difference between the Fermi level and the bottom of the valence band of GeSe is 0.27 eV, and the difference between the Fermi level and the top of the conduction band of MoS$_2$ is 0.38 eV. They are derived from the formulas: $n = (g_{2D}k_BT)ln\{1 + exp[(E_F-E_C)/k_BT]\}$ and $p = (g_{2D}k_BT)ln\{1 + exp[-(E_F-E_V)/k_BT]\}$, where g_{2D} is 2D density of states in TMD semiconductor. The carrier density n and p are calculated
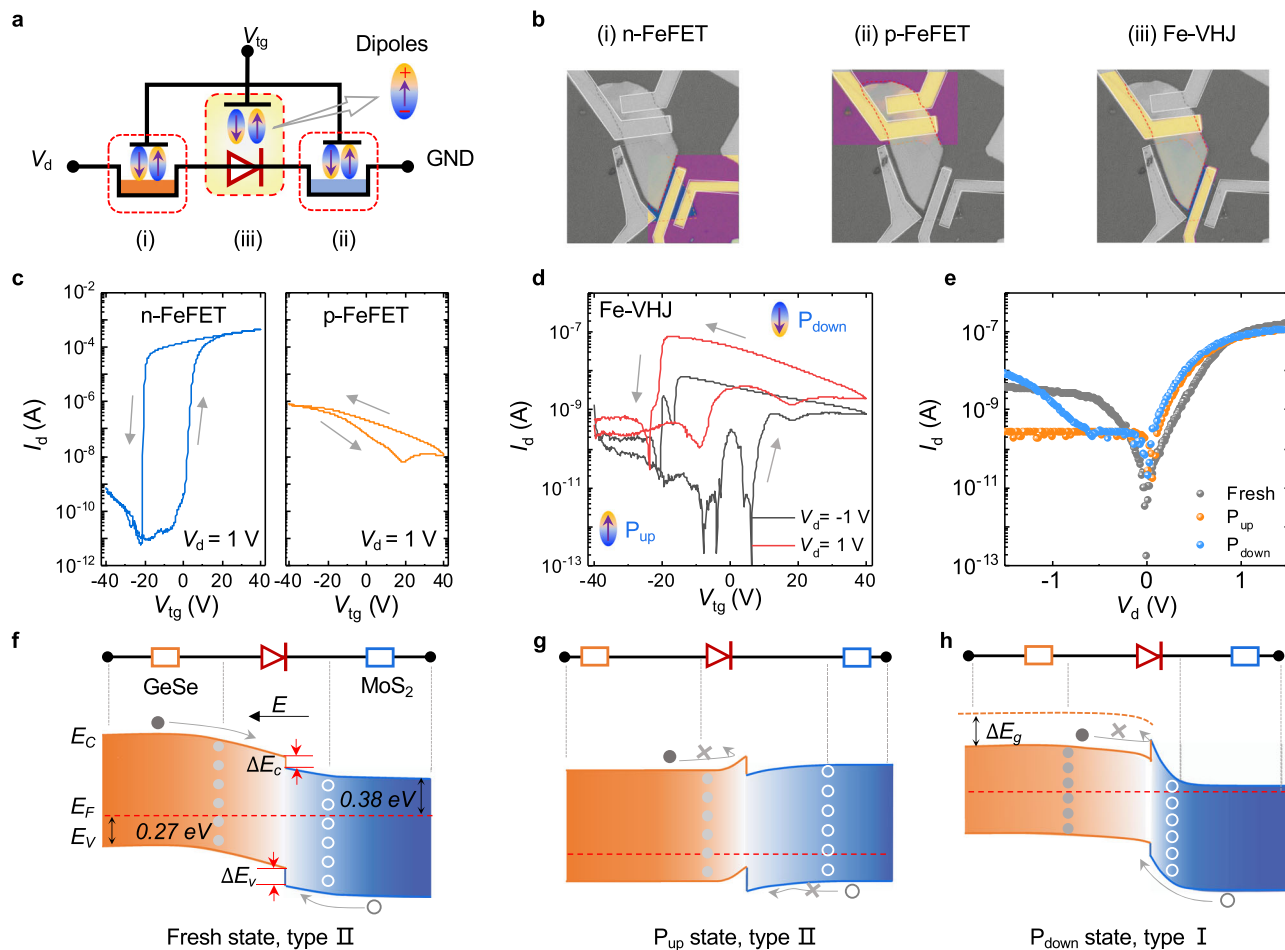
Fig. 2 Electrical properties of GeSe/MoS₂ heterojunction tuned by the ferroelectric polymer P(VDF-TrFE). a Electrical configuration of the device, with three parts represented in the dashed-line frames. **b** Optical image of three device elements: MoS₂ n-FeFET, GeSe p-FeFET, and GeSe/MoS₂ Fe-VHJ. **c** Transfer characteristics of GeSe p-FeFET and MoS₂ n-FeFET at $V_d = 1$ V. **d** Transfer characteristics of the Fe-VHJ under forward and reverse biases. **e** Output characteristics of the GeSe/MoS₂ heterojunction when P(VDF-TrFE) are fresh, polarized upward, and polarized downward states. **f** Schematic of the energy band structure of the GeSe/MoS₂ junction at "Fresh" state. E_F-E_C and E_F-E_v were calculated using experimental data. Schematic of the heterojunction energy bands at an equilibrium state. Bandgap evolution of the GeSe/MoS₂ Fe-VHJ at **g** "P_up" state and **h** "P_down" state.

by $n(p) = \sigma/\mu e$, where conductivity σ and mobility μ are extracted from the output and transfer curves in Supplementary Fig. 2. The calculation details are displayed in Supplementary Note 3. Consequently, the difference between the Fermi levels of these two materials can be calculated to be 0.35 eV before they contact. At P_up state, holes in GeSe are accumulated and electrons in MoS₂ are depleted, leading to the band bending upward in GeSe. The drift current of minority carriers in both sides is restricted, resulting in suppression of reverse current. The reverse current is approximately 0.2 nA, lower than that at the Fresh state. When P(VDF-TrFE) is polarized down, the reverse current is suppressed under small bias but increases under larger bias. The increased current is generated from Fowler–Nordheim tunneling as fitted in Supplementary Fig. 10, indicating the existence of a triangle barrier on the conduction band. The triangle barrier may result from the bandgap reduction of GeSe at P_down state. Generally, an electrical field narrows the bandgap of semiconductors by shifting the conduction band minimum downward while the conduction band maximum is nearly a constant[27,41]. Thus, the band structure evolution of GeSe changes the conduction band offset from 0.10 eV to a negative value thus type I (straddling) band alignment is formed. Although the band offset ΔE_c is a small value, it has an effective impact on carrier transport as shown in the temperature-dependent electrical properties in Supplementary Fig. 9. Hereto,

based on these electrical analyses, it is verified that the band alignment of the GeSe/MoS₂ can be effectively tuned by the ferroelectric field. According to the Debye length of GeSe, the tunability of ferroelectric field can still work on thicker GeSe as analyzed in Supplementary Note 4.

Performance of photovoltaic response. To characterize the photodetection performance of GeSe/MoS₂ Fe-VHJ, we tested its photoresponse from visible to near-infrared. To ensure a low and stable dark current, the P(VDF-TrFE) polymer is polarized up. As presented in Fig. 3a, the heterojunction demonstrates ultra-low dark current at $V_d = 0$ V and embraces highly sensitive photoresponse to 520 nm illumination with different incident light power. The I_d−V_d characteristics under different illumination intensities at P_up and P_down states are shown in Fig. 3b, c, respectively. The injection of photo-generated carriers makes the I_d−V_d curves shift, resulting in short-circuit current (I_{sc}) and open-circuit voltage (V_{oc}). The V_{oc} reaches 0.49 V at P_up state that is larger than 0.37 V of P_down state. The difference of V_{oc} indicates that the difference of Fermi levels is tuned by the electric field originated from ferroelectric polarization. Moreover, the dark current is suppressed at P_up state, leading to a larger photoswitching on/off ratio and improving the sensitivity. Therefore, the
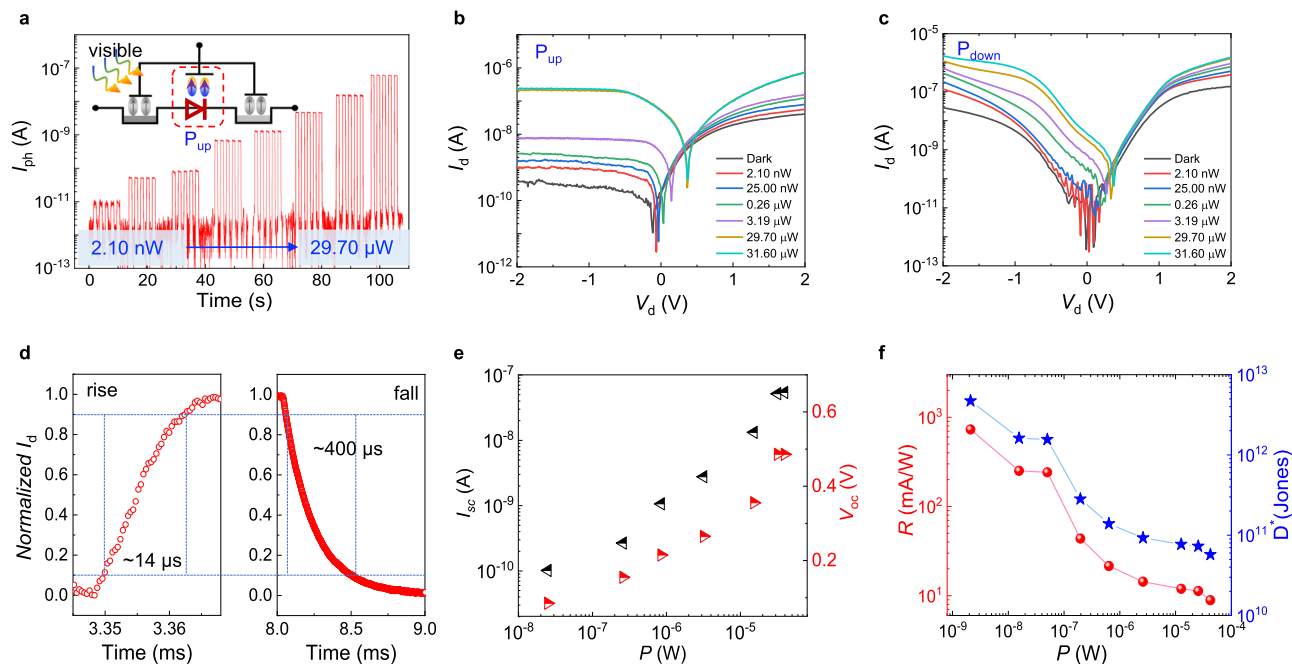
Fig. 3 Photoresponse performance of GeSe/MoS₂ Fe-VHJ in the visible region. a Time-resolved photocurrent in the "P$_{up}$" state with 520 nm incident light and power are 2.10 nW, 25.00 nW, 50.10 nW, 0.26 μW, 0.85 μW, 3.19 μW, 15.30 μW, and 29.70 μW, respectively. The light power is the fraction on the heterojunction. Output characteristics under different light powers at **b** "P$_{up}$" state and **c** "P$_{down}$" state. **d** In all, 10–90% photocurrent rise and decay times derived with λ = 520 nm illumination. **e** Power dependency of short-circuit current and open-circuit voltage with an incident light wavelength of 520 nm. **f** Photoresponsivity and detectivity of GeSe/MoS₂ Fe-VHJ.

Fe-VHJ shows a better photovoltaic response at P$_{up}$ state, where GeSe/MoS₂ forms a type II band alignment. As shown in Fig. 3d, the photocurrent rise time is as short as 14 μs and the fall time is 400 μs. The trap in thick GeSe is a factor limiting the response speed because it can induce photogating effect that prolonged the photo-generated carriers. Besides, the defective interfacial layer between GeSe and MoS₂ may make a negative effect on the response speed too. I_{sc} and V_{oc} increased with the power of 520 nm light illumination, as indicated in Fig. 3e. When the device is saturated-absorption, they reach maximum values of 52 nA and 0.49 V. Figure 3f shows the power-dependence of photo-responsivity (R) and detectivity (D^*) at $V_d = 0$ V. Photo-responsivity is calculated using the formula $R = I_{ph}/P$. In a photodiode, the thermal noise and the generation-recombination (g-r) noise can all be ignored because the carriers are depleted in the space charge region. The shot noise in the current passing through the junction is the intrinsic noise. So the detectivity of GeSe/MoS₂ photovoltaic detector can be calculated by $D^* = A^{1/2}R/(2eI_{dark})^{1/2}$, where A is the effective area of the photodetector (2×10^{-6} cm²), e is the elementary electronic charge, and I_{dark} is the dark current (1.5 pA). The photodetector achieves maximum photoresponsivity and detectivity values of 729.3 mA/W and 4.7×10^{12} Jones under the illumination of 520 nm light with 2.1 nW. To verify the specific value of the GeSe/MoS₂ hetero-junction, we measured the noise current spectrum at room temperature, as shown in Supplementary Fig. 11. The noise is directly measured allowing D^* to be calculated as $D^* = (A\Delta f)^{1/2}/NEP$, where Δf is the integration time (1 s) and NEP is noise equivalent power (defined by in i_n/R, where R is the responsivity, and i_n is the measured noise current)[42]. The measured low-frequency noise equivalent power can reach a value of 1.37×10^{-15} WHz$^{-1/2}$. From this measurement, we find a D^* value of 1.03×10^{12} cm Hz$^{1/2}$ W^{-1}. This value is in good agreement with the result above. The small difference can be attributed to weak generation-recombination noise generated in the thick GeSe.

Photoresponse in NIR of GeSe/MoS₂ Fe-VHJ. In commercial integrated photonics based on Si or Ge, transceivers, modulators, and detectors operate at a wavelength between 1300 and 1550 nm (corresponding $E_{opt} \approx 0.8$ eV)[43–45]. According to the bandgaps of MoS₂ (1.2 eV) and GeSe (1.1 eV), however, the application in integrated photonics of the GeSe/MoS₂ heterojunction is spec-trally limited. Nevertheless, with the Stark effect induced by the giant ferroelectric field on GeSe, the GeSe/MoS₂ Fe-VHJ is sen-sitive to photons with lower energy. As demonstrated by the transfer curves at $V_d = -1$ V with/without 1550 nm light illu-mination plotted in Fig. 4a, photocurrent is generated when gate voltage sweeps from 0 V to 40 V and 40 V to −20 V, where P (VDF-TrFE) is polarized down and the GeSe/MoS₂ heterojunc-tion is type I alignment. A similar response is observed in transfer curves at $V_d = 1$ V. Photocurrent maps confirm the sensitivity of the whole GeSe area under near-infrared irradiation (Supple-mentary Fig. 12), while only the overlapping heterojunction part shows sensitivity to visible light. This indicates that the photo-current is generated in the GeSe part with Stark effect works. In addition, the photocurrent switching characteristics under the illumination of 1310 and 1550 nm are shown in Fig. 4b, c, respectively. The GeSe/MoS₂ Fe-VHJ shows stable photocurrent switching characteristics at both reverse and forward biases. In contrast to the response to visible light, the response to NIR light with assistance of an external bias is much slower (see Supple-mentary Fig. 13) because the device operates in a photo-conductive mode in the near-infrared region. The energy band diagrams of GeSe/MoS₂ VHJ under various biases when P(VDF-TrFE) is polarized down are shown in Fig. 4d. At equilibrium state, photo-generated carriers in GeSe cannot overcome the peak in the conduction band, falling to be collected by electrodes. With a reverse bias applied across the outer electrodes, the peak barrier is covered by the steep band structure and no longer affects the transport of electrons. Correspondingly, the band offset in the valence band is also negligible for collecting photo-generated
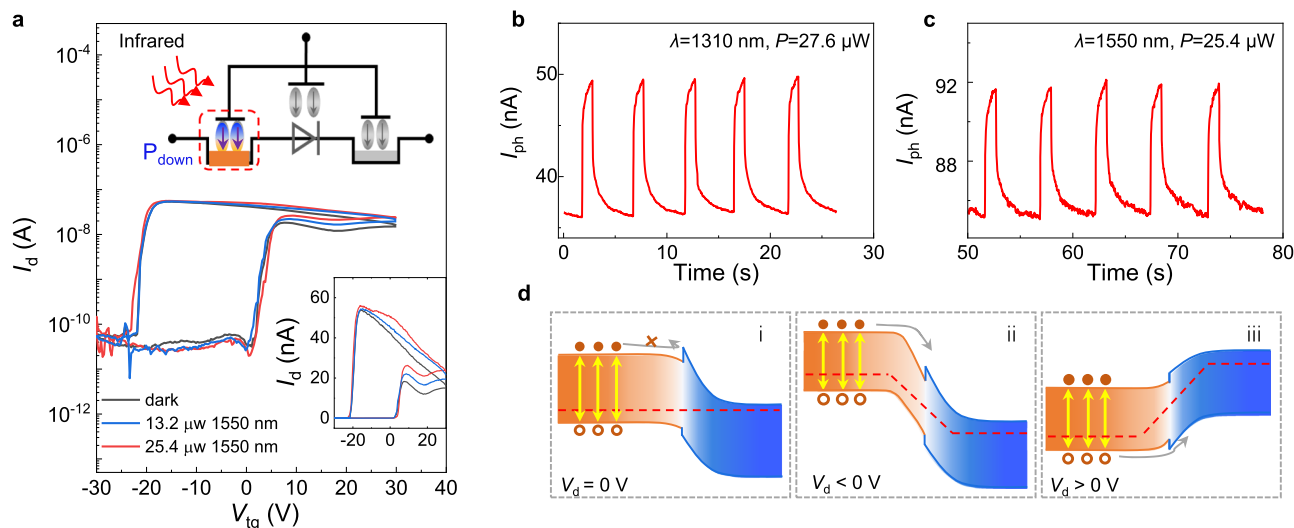
Fig. 4 Photoresponse in near-infrared spectroscopy. a Transfer curves under the illumination of 1550 nm light at $V_d = 1$ V. Time-resolved photocurrent with incident light wavelengths of **b** 1310 nm (P_{down} state, $V_d = -1$ V) and **c** 1550 nm (P_{down} state, $V_d = 1$ V). **d** Transport of the carriers generated by infrared light in GeSe/MoS$_2$ Fe-VHJ at (i) equilibrium state, (ii) reverse bias, and (iii) forward bias.
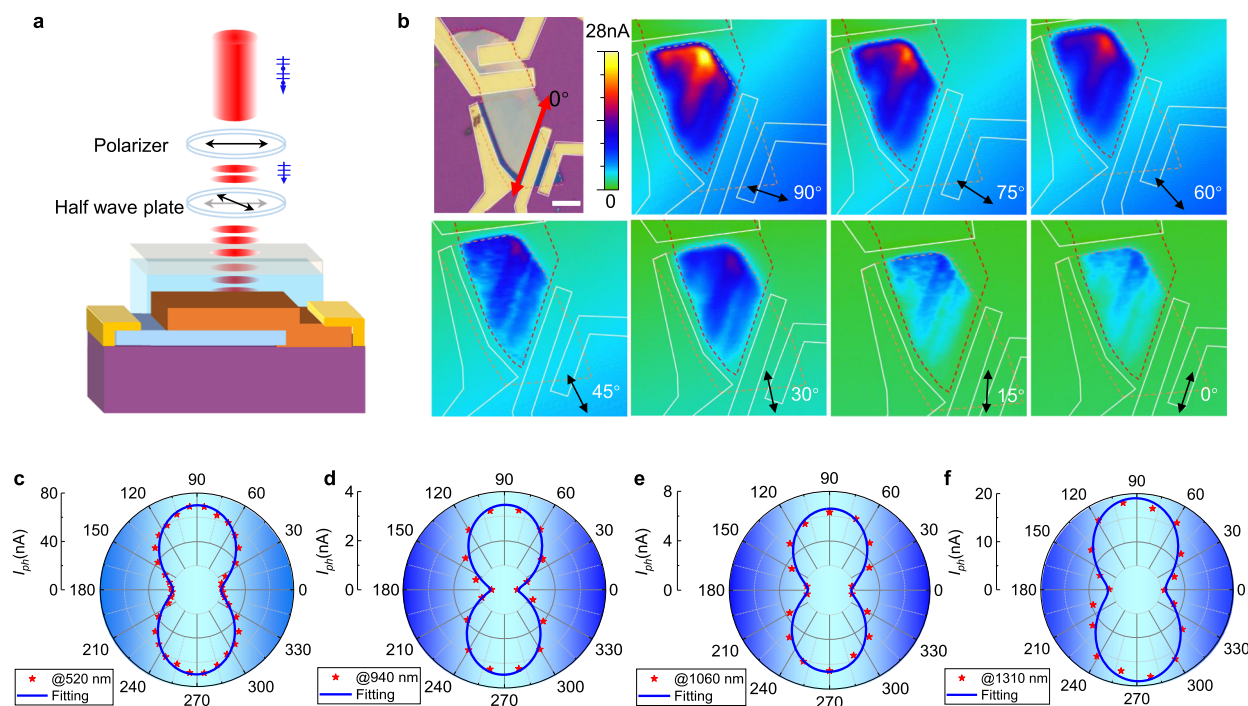

Fig. 5 Polarization detection characteristics of the GeSe/MoS$_2$ Fe-VHJ. a Schematic of the test setup. **b** Photocurrent mapping of the GeSe/MoS$_2$ Fe-VHJ. **c**–**f** Photocurrent as a function of the incident light polarization angle. The wavelength ranges from visible to near-infrared wavelengths (520, 940, 1060, and 1310 nm). The solid line represents fitting using a sinusoidal function $I_{ph}(\delta) = I_{py} \cos^2(\delta + \varphi) + I_{px} \sin^2(\delta + \varphi)$. The fitted dichroic ratios under different wavelengths are 5.53, 6.25, 3.80, and 3.16.

holes when a high enough forward bias is applied. As a result, the photocurrent generated by infrared light can only be collected with a large enough bias. Therefore, band alignment evolution in GeSe/MoS$_2$ FeFET broadens the detective range and makes its potential application in telecommunication based on photonic integrated circuits.

Polarization-resolved sensitivity of GeSe/MoS$_2$ Fe-VHJ. Photodetectors are essential sensing tools for acquiring light information of the environment. With the development of artificial

intelligence, more accurate information must be acquired and analyzed. Anisotropic materials such as black phosphorus (BP), ReS$_2$, ReSe$_2$, and GeSe have been successively employed to develop polarization detectors[46–48]. Among these materials, GeSe is a promising and rare *p*-type semiconductor that can form ideal *pn* junctions with *n*-type 2D materials[33,49]. More importantly, GeSe has a direct bandgap for high-efficiency absorption[50]. As shown in Fig. 5, the polarization-dependent photoresponse of the GeSe/MoS$_2$ Fe-VHJ is comprehensively studied. The test setup is illustrated in Fig. 5a. The incident light was emitted

perpendicularly onto the device and polarized using a Glan–Taylor prism. By rotating the half-wave plate, the polarization angle of the linearly polarized light was altered, but the laser power remained stable. To determine the effective photoresponse area, we performed photocurrent mapping on the device. In addition, we measured the fluctuation of photocurrent to different angles of incident light. The results are presented in Fig. 5b. P(VDF-TrFE) maintains an upward polarization field during scanning, and no bias is applied to the GeSe/MoS$_2$ heterojunction. Zero degree is set along with the direction of a cleavage side of GeSe. The photocurrent mappings are successively obtained from 0° to 90° by steps of 15°. The photocurrent intensity varies noticeably with the incident polarization angle. The most significant photoresponse is achieved at 90° and the weakest at 0°. According to the device configuration, the response area is the overlapping part of GeSe and MoS$_2$, indicating that these two materials formed an effective *pn* junction. The specific relationship between photocurrent and polarization angle must be discovered to quantitatively characterize the polarization sensitivity of the device. Figure 5c–f shows the relationship between the photocurrent and polarization angle of the device from the visible to near-infrared wavelength (520, 940, 1060, and 1310 nm), respectively. The photocurrent varies periodically with the angle of incident polarized light. Fitting with the sine function $I_{ph}(\delta) = I_{py} \cos^2(\delta + \varphi) + I_{px} \sin^2(\delta + \varphi)$, the device dichroic ratio I_{py}/I_{px} could be obtained to determine the polarization detection capability of the device; the dichroic ratios of the device under the illumination of 520, 940, 1060, and 1310 nm are 5.53, 6.25, 3.80, and 3.16, respectively. These parameters are higher compared to GeSe photodetectors and other anisotropic devices (shown in Supplementary Table 1)[46,51,52]. The enhancement of the dichroism of GeSe possibly originates from the anisotropic stark effect in GeSe[53]. The GeSe/MoS$_2$ Fe-VHJ is a promising polarization-sensitive photodetector for optical sensing.

In conclusion, we have designed a proof-of-concept device architecture, the GeSe/MoS$_2$ Fe-VHJ. The carrier transport of the heterojunction can be effectively tuned by the ferroelectric polarization field with band alignment evolution. The device demonstrates quick and sensitive responsivity to visible incident light. Besides, the Fe-VHJ is sensitive in the near-infrared region as well because of the band engineering of ferroelectric dipoles. Ultimately, we used this single device to obtain the intensity and polarization information of light. Our high-performance Fe-VHJ is a pioneering integrated sensing device.

Methods

Device fabrication. MoS$_2$ and GeSe are exfoliated from bulk materials and transferred on a p-doped silicon substrate covered with 285 nm silicon oxide. Then the chosen GeSe flake was picked up by water-soluble poly(vinyl alcohol) film. The electrodes were defined by electron beam lithography and Ti/Au (15 nm/50 nm) were deposited by thermal evaporation. The P(VDF-TrFE) (70:30 in mol%) was spin-coated on the substrate and annealed at 135 °C for 4 h. The top gate electrode is patterned by a metal mask and 9 nm aluminum was deposited. The top gate is nearly transparent to avoid affecting the light absorption efficiency as shown in Supplementary Fig. 14.

Electrical and photoelectronic characterization. The electrical measurements were performed by Agilent B2912A and Keysight B1500A at room temperature. The photoresponse measurement was under monochromatic light sources with a spot diameter of about 100 μm to ensure a uniform power on the device. The photocurrent mapping was carried out by a modulated scanning laser beam and the photocurrent signal was acquired by a lock-in amplifier. The response time was measured by a high-speed Tektronix MDO3014 oscilloscope.

Data availability

The authors declare that the data that support the graphs within this paper are available from the corresponding author upon reasonable request. Source data are provided with this paper.

References

1. Matthews, J. et al. Defects in epitaxial multilayers: I. Misfit dislocations. *J. Cryst. Growth* **27**, 118–125 (1974).
2. Matthews, J. et al. Defects in epitaxial multilayers: III. Preparation of almost perfect multilayers. *J. Cryst. Growth* **32**, 265–273 (1976).
3. Vallet, M. et al. Highly strained AlAs-type interfaces in InAs/AlSb heterostructures. *Appl. Phys. Lett.* **108**, 211908 (2016).
4. Qing Hua, W. et al. Electronics and optoelectronics of two-dimensional transition metal dichalcogenides. *Nat. Nanotechnol.* **7**, 699–712 (2012).
5. Novoselov, K. S. et al. Electric field effect in atomically thin carbon films. *Science* **306**, 666–669 (2004).
6. Ferrari, A. C. et al. Raman spectrum of graphene and graphene layers. *Phys. Rev. Lett.* **97**, 187401 (2006).
7. Seyler, K. L. et al. Signatures of moire-trapped valley excitons in MoSe$_2$/WSe$_2$ heterobilayers. *Nature* **567**, 66–70 (2019).
8. Liu, Y. et al. Van der Waals integration before and beyond two-dimensional materials. *Nature* **567**, 323–333 (2019).
9. Cao, Y. et al. Unconventional superconductivity in magic-angle graphene superlattices. *Nature* **556**, 43–50 (2018).
10. Cao, Y. et al. Correlated insulator behaviour at half-filling in magic-angle graphene superlattices. *Nature* **556**, 80–84 (2018).
11. Furchi, M. M. et al. Photovoltaic effect in an electrically tunable van der Waals heterojunction. *Nano Lett.* **14**, 4785–4791 (2014).
12. Woo Jong, Y. et al. Highly efficient gate-tunable photocurrent generation in vertical heterostructures of layered materials. *Nat. Nanotechnol.* **8**, 952–958 (2013).
13. Withers, F. et al. Light-emitting diodes by band-structure engineering in van der Waals heterostructures. *Nat. Mater.* **14**, 301–306 (2015).
14. Li, D. et al. Two-dimensional non-volatile programmable p–n junctions. *Nat. Nanotechnol.* **12**, 901–906 (2017).
15. Liu, C. et al. A semi-floating gate memory based on van der Waals heterostructures for quasi-non-volatile applications. *Nat. Nanotechnol.* **13**, 404–410 (2018).
16. Britnell, L. et al. Resonant tunnelling and negative differential conductance in graphene transistors. *Nat. Commun.* **4**, 1794 (2013).
17. Yan, R. et al. Esaki diodes in van der Waals heterojunctions with broken-gap energy band alignment. *Nano Lett.* **15**, 5791–5798 (2015).
18. Shim, J. et al. Phosphorene/Rhenium disulfide heterojunction-based negative differential resistance device for multi-valued logic. *Nat. Commun.* **7**, 13413 (2016).
19. Yan, X. et al. Tunable SnSe$_2$/WS heterostructure tunneling field effect transistor. *Small* **13**, 1701478 (2017).
20. Fan, S. et al. Tailoring quantum tunneling in a vanadium-doped WSe$_2$/SnSe$_2$ heterostructure. *Adv. Sci.* **7**, 1902751 (2020).
21. Lee, J. et al. Modulation of junction modes in SnSe$_2$/MoTe$_2$ broken-gap van der Waals heterostructure for multifunctional devices. *Nano Lett.* **20**, 2370–2377 (2020).
22. Yang, T. et al. Ultrahigh-performance optoelectronics demonstrated in ultrathin perovskite-based vertical semiconductor heterostructures. *ACS Nano* **13**, 7996–8003 (2019).
23. Ko, C. et al. Ferroelectrically gated atomically thin transition-metal dichalcogenides as nonvolatile memory. *Adv. Mater.* **28**, 2923–2930 (2016).
24. Wu, G. et al. Programmable transition metal dichalcogenide homojunctions controlled by nonvolatile ferroelectric domains. *Nat. Electron.* **3**, 43–50 (2020).
25. Wang, X. et al. Ultrasensitive and broadband MoS2 photodetector driven by ferroelectrics. *Adv. Mater.* **27**, 6575–6581 (2015).
26. Liu, Y. et al. Gate-tunable giant stark effect in few-layer black phosphorus. *Nano Lett.* **17**, 1970–1977 (2017).
27. Deng, B. et al. Efficient electrical control of thin-film black phosphorus bandgap. *Nat. Commun.* **8**, 14474 (2017).
28. Chu, T. et al. Electrically tunable bandgaps in bilayer MoS2. *Nano Lett.* **15**, 8000–8007 (2015).
29. Zibouche, N. et al. Transition-metal dichalcogenide bilayers: switching materials for spintronic and valleytronic applications. *Phys. Rev. B* **90**, 125440 (2014).
30. Si, M. et al. A ferroelectric semiconductor field-effect transistor. *Nat. Electron.* **2**, 580–586 (2019).
31. Ni, K. et al. Ferroelectric ternary content-addressable memory for one-shot learning. *Nat. Electron.* **2**, 521–529 (2019).
32. Chen, Y. et al. Optoelectronic properties of few-layer MoS$_2$ FET gated by ferroelectric relaxor polymer. *ACS Appl. Mater. Inter.* **8**, 32083–32088 (2016).

33. Yap, W. C. et al. Layered material GeSe and vertical $GeSe/MoS_2$ p-n heterojunctions. *Nano Res.* **11**, 420–430 (2017).

34. Bullock, J. et al. Polarization-resolved black phosphorus/molybdenum disulfide mid-wave infrared photodiodes with high detectivity at room temperature. *Nat. Photon* **12**, 601–607 (2018).

35. Ubrig, N. et al. Design of van der Waals interfaces for broad-spectrum optoelectronics. *Nat. Mater.* **19**, 299–304 (2020).

36. Wilson, N. R. Determination of band offsets, hybridization, and exciton binding in 2D semiconductor heterostructures. *Sci. Adv.* **3**, 1601832 (2017).

37. Pierucci, D. et al. Band alignment and minigaps in monolayer MoS_2-graphene van der Waals heterostructures. *Nano Lett.* **16**, 4054–4061 (2016).

38. Chiu, M. H. et al. Determination of band alignment in the single-layer MoS_2/WSe_2 heterojunction. *Nat. Commun.* **6**, 6 (2015).

39. Xu, Y. et al. Contacts between two- and three-dimensional materials: Ohmic, Schottky, and p-n heterojunctions. *ACS Nano* **10**, 4895–4919 (2016).

40. Chen, X. et al. Widely tunable black phosphorus mid-infrared photodetector. *Nat. Commun.* **8**, 1672 (2017).

41. Qiu, Z. et al. Giant gate-tunable bandgap renormalization and excitonic effects in a 2D semiconductor. *Sci. Adv.* **5**, 2347 (2019).

42. Long, M. et al. Room temperature high-detectivity mid-infrared photodetectors based on black arsenic phosphorus. *Sci. Adv.* **3**, 1700589 (2017).

43. Romagnoli, M. et al. Graphene-based integrated photonics for next-generation datacom and telecom. *Nat. Rev. Mater.* **3**, 392–414 (2018).

44. Bie, Y. Q. et al. A MoTe2-based light-emitting diode and photodetector for silicon photonic integrated circuits. *Nat. Nanotechnol.* **12**, 1124–1129 (2017).

45. Dumas, D. C. S. et al. Ge/SiGe quantum confined Stark effect electro-absorption modulation with low voltage swing at $\lambda = 1550$ nm. *Opt. Express* **22**, 19284–19292 (2014).

46. Liu, F. et al. Highly sensitive detection of polarized light using anisotropic 2D ReS_2. *Adv. Func. Mater.* **26**, 1169–1177 (2016).

47. Wang, X. et al. Short-wave near-infrared linear dichroism of two-dimensional Germanium Selenide. *J. Am. Chem. Soc.* **139**, 14976–14982 (2017).

48. Shi, G. Anisotropic spin transport and strong visible-light absorbance in few-layer SnSe and GeSe. *Nano Lett.* **15**, 6926–6931 (2015).

49. Xue, D. J. et al. GeSe thin-film solar cells fabricated by self-regulated rapid thermal sublimation. *J. Am. Chem. Soc.* **139**, 958–965 (2017).

50. Xu, Y. et al. First-principles study on the electronic, optical, and transport properties of monolayer α- and β-GeSe. *Phys. Rev. B* **96**, 245421 (2017).

51. Ye, L. et al. Highly polarization sensitive infrared photodetector based on black phosphorus-on-WSe2 photogate vertical heterostructure. *Nano Energy* **37**, 53–60 (2017).

52. Li, X. K. et al. Polarization-dependent photocurrent of black phosphorus/rhenium disulfide heterojunctions. *Adv. Mater. Inter.* **5**, 1701605 (2018).

53. Kim, J. et al. Observation of tunable band gap and anisotropic Dirac semimetal state in black phosphorus. *Science* **349**, 723–726 (2015).

Author contributions

Y. C. and X.-D. W. contributed equally to the work. J. W. and Y. C. conceived the idea for the project and designed the experiments. J. W. supervised the project. Z.-M. W. and X.-T. W. synthesized the GeSe crystal. Y. C. and X.-D. W. fabricated devices and performed electrical measurements. Y. C., W. H., Z. W., W. J., F. W., P. W., Y. J., and B. W. performed optical measurement. H. L. and Z.-M. W. carried out the calculated part. Y. C., X.-D. W., T. L., H. S., W. H., X. M., and J. C. analyzed the data. J. W., Y. C., and X.-D. W. co-wrote the manuscript. All authors discussed the results and commented on the manuscript.

Competing interests

The authors declare no competing interests.

Additional information

Supplementary information The online version contains supplementary material available at https://doi.org/10.1038/s41467-021-24296-1.

Correspondence and requests for materials should be addressed to Z.W., W.H. or J.W.

Peer review information *Nature Communications* thanks Peixin Zhang and the other, anonymous, reviewer(s) for their contribution to the peer review of this work.

Reprints and permission information is available at http://www.nature.com/reprints

Publisher's note Springer Nature remains neutral with regard to jurisdictional claims in published maps and institutional affiliations.